IEEE Access
Multidisciplinary ⋮ Rapid Review ⋮ Open Access Journal

Received July 15, 2020, accepted July 27, 2020, date of publication July 30, 2020, date of current version August 11, 2020.

Digital Object Identifier 10.1109/ACCESS.2020.3013068

A Compact Hemispherical Beam-Coverage Phased Array Antenna Unit for 5G mm-Wave Applications

JIHOON BANG AND JAEHOON CHOI, (Senior Member, IEEE)
Department of Electronics and Computer Engineering, Hanyang University, Seoul 133-791, South Korea

Corresponding author: Jaehoon Choi (choijh@hanyang.ac.kr)

This work was supported in part by the Human Resources Development Program of the Korea Institute of Energy Technology Evaluation and Planning (KETEP) funded by the Korea Government Ministry of Trade, Industry and Energy under Grant 20194010201860, and in part by the Institute of Information and Communications Technology Planning and Evaluation (IITP) funded by the Korea Government through the Ministry of Science and ICT (MSIT) (Fundamental Research for Solving the Bottleneck Technology of Millimeter Wave 5G Cellular Array Antenna) under Grant 2018-0-00732.

ABSTRACT A compact low-profile phased array antenna unit with unidirectional hemispherical beam-coverage for 5G mm-wave applications is proposed in this paper. A four-subarray configuration is used for the proposed structure to achieve unidirectional hemispherical coverage in the boresight direction normal to the substrate. An artificial magnetic conductor (AMC)-backed slot antenna array with an optimal separation distance of 1.9 mm (= 0.31 λ at 28 GHz) is proposed as a subarray. The proposed antenna has increased *H*-plane beamwidth with the measured peak gain of 11.62 dBi and provides the desired wide inclined beam pattern in the elevation plane. The proposed antenna also offers steered beams over the range within ±45° in the azimuth plane. The hemispherical-coverage, phased array antenna unit composed of the four designed subarrays has overall dimensions of 80.8 mm × 80.8 mm × 2.4 mm. The coverage efficiencies of the proposed phased array antenna unit are 0.82, 0.71, and 0.61 for threshold gains of 5 dBi, 8 dBi, and 10 dBi, respectively, where the maximum solid angle is 2π steradians.

INDEX TERMS 5G mm-wave, phased array antenna, hemispherical coverage, artificial magnetic conductor backed slot antenna, coverage enhancement.

I. INTRODUCTION

With the explosive growth of mobile data traffic over the last few years, the demands for higher data-rate services have risen sharply. To cope with this growing need, fifth-generation (5G) mobile communication that promises a data rate of several gigabits per second and which tolerates millisecond latency was envisioned [1], [2]. A key technology that allows for the evolution of data speed and network capacity on 5G systems is the use of millimeter-wave (mm-wave) bands with large spectrum resources. Recently, four frequency bands, including the 26 GHz, 28 GHz, and 39 GHz bands in frequency range 2 (FR2), have been arranged for 5G new radio (NR) in the 3GPP 5G specification (Release 15) [3]. However, these mm-wave bands suffer from relatively severe propagation losses which impair communication performance [4]. Hence, array antennas with a high gain are required to mitigate the propagation attenuation. Since a high gain leads to a narrow radiation beamwidth and thus limits the angular coverage, directional phased array antennas having an electrical beam-steering capability are usually proposed for implementation at both the base station and mobile device [5], [6]. Even though the basic issue of angular coverage can be mitigated by steering the beam, it remains challenging to achieve a sufficiently wide angular coverage using one phased array. An exception is the application of a macro cell base station as in [7] and [8], which has no restriction on space and the number of antenna elements. According to [9]–[12], regardless of the radiating element type, single 4 × 1 and 8 × 1 uniform linear arrays (ULAs) have spatial coverage efficiencies, as defined by [10], under 25% and 50%, respectively, for $G_{th} \geq 8$ dBi, where G_{th} represents the threshold antenna gain. Several studies have been carried out to improve the spatial coverage efficiency by arranging multiple subarrays, each of which mainly consists of ULAs, within one phased

The associate editor coordinating the review of this manuscript and approving it for publication was Lu Guo.

array antenna unit. In [13]–[15], techniques in which three subarrays were mounted on different sides of the edge region of a printed circuit board (PCB) were reported. In [16], three slot subarrays were implemented on the same plane of the metallic chassis to utilize the surface wave excited on the metal plate. Moreover, reconfigurable phased array units with a combination of broadside and end-fire radiations [17]–[19] and controlled pin-diodes [20] have been presented. These studies have effectively improved spatial coverage efficiency by achieving 360° spherical beam-coverage, and therefore they are promising candidate techniques for mm-wave 5G mobile handsets.

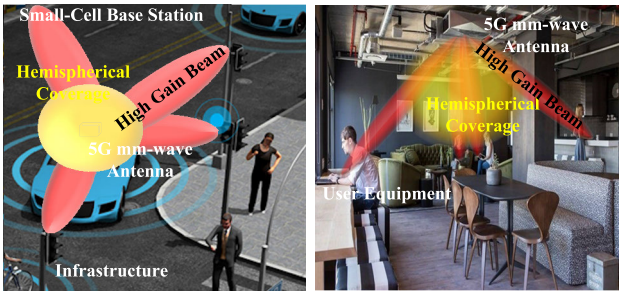

FIGURE 1. Several representative mm-wave 5G wireless service applications requiring the hemispherical beam-coverage: (a) the vehicle-to-infrastructure communication and (b) the indoor access point.

Nevertheless, the coverage issue has remained for some scenarios in mm-wave 5G wireless services, such as vehicle-to-infrastructure (V2I)/high-speed train (HST)/air-to-ground (A2G) communications [21]–[24], indoor access points (AP) [25], and small-cell base transmit systems (BTS) [26] shown in Fig. 1. Since there is no need for back radiation in those specific applications, 180° unidirectional hemispherical beam-coverage is preferred to 360° spherical coverage. However, the coverage range of phased array units with a specific subarray or reconfigurable configurations cannot be varied freely. If adopting the subarray configurations presented in previous work [13]–[15], [17]–[20] designed for mobile handsets, the desired complete unidirectional broadside hemispherical coverage is difficult to achieve. This is because, due to structural limitations, the unnecessary back radiation is included outside of hemispherical area when using three subarrays. In addition, the boresight direction of the hemispherical coverage area of those phased array units is parallel to the antenna substrate instead of normal to it. This gives phased array antenna units a high-profile, making them difficult to integrate with the systems for the aforementioned mm-wave applications.

In this paper, to address this issue, we propose a compact low-profile phased array antenna unit with the desired unidirectional hemispherical beam-coverage for the aforementioned 5G mm-wave applications. The design concept of the proposed phased array antenna unit is shown in Fig. 2. Four subarrays are shown to be composed of the phased array unit, and each subarray is designed to cover a quarter of

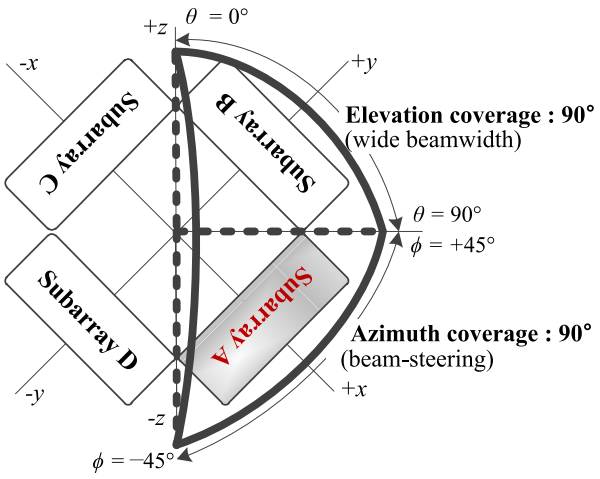

FIGURE 2. Design concept diagram of the proposed hemispherical beam-coverage phased array antenna unit composed of four subarrays.

the upper hemisphere with moderate-high gain. Therefore, one subarray has 90° coverage for both the elevation and azimuth planes. For this, the beam is steered over the range within ±45° in the azimuth plane, and the wide inclined beam is formed over the range of 0°–90° in the elevation plane, where the maximum gain will appear in the vicinity of 45° in the θ angle. In addition, a good front-to-back ratio (FBR) and isolations between elements are needed for the antenna design.

This paper is organized into four sections. The theoretical analysis of the subarray design, a performance assessment using full-wave electromagnetic simulation software, and experimental proof is presented in Section II. The overall design and performance of the proposed hemispherical beam-coverage phased array antenna unit are presented in Section III. The conclusion is discussed in Section VI.

II. SUBARRAY DESIGN

Based on the design concept described in Section I, the key design considerations to be satisfied for each subarray are summarized as follows.

A. High Gain and Unidirectional Radiation
($G_{max} \geq 10$ dBi and FBR ≥ 10 dB)
B. Quarter-Hemispherical Coverage
($\eta_c \geq 0.7$ for $G_{th} > 8$ dBi)
a. Steered Beam for Azimuth (for $-45° \geq \phi \geq +45°$)
b. Wide Inclined Beam for Elevation (for $0° \geq \theta \geq +90°$)
C. Compact and Low-Profile Structure
D. Good Reflection Coefficients and Mutual Couplings
(≤ -10 dB over the targeted band of 28 GHz – 29 GHz)

For a subarray design that meets those requirements simultaneously, we devise an AMC-backed slot antenna array with an optimal separation distance between the AMC surface and the antenna elements. In this chapter, we deal with the subarray design in stages. We first describe the antenna element design in Section IIA and then provide the array

design in Section IIB. The theoretical analysis, the design configuration, and the results are also included in those sections. The overall phased array unit will be discussed in detail in the next chapter.

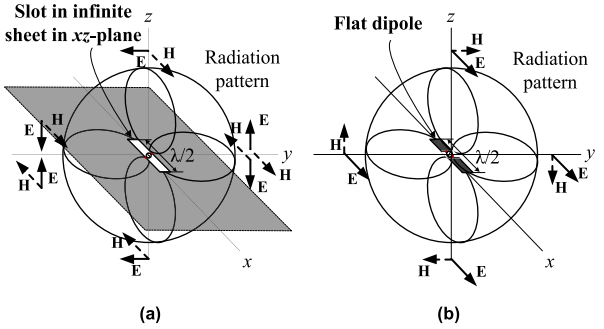

FIGURE 3. Radiation field patterns: (a) slot in an infinite sheet and (b) of complementary dipole antenna.

A. ANTENNA ELEMENT DESIGN

1) SLOT ANTENNA

It was demonstrated by Booker [27] that an ideal thin slot inserted into a perfectly conducting sheet of infinite extent and a complementary dipole antenna have the same radiation pattern but with interchanged E- and H-fields, as shown in Fig. 3 [28]. When the half-wavelength slot inserted into the infinite flat sheet is positioned on the xy-plane at $z = 0$ and is in the x-direction as in Fig. 3(a), the electric field patterns at far-field observation points are denoted as

$$E(\theta) = \mathrm{A}\left[\frac{\cos(\pi/2\cos\theta)}{\sin\theta}\right], \quad \text{for } \phi = 0^\circ \tag{1}$$

$$E(\theta) = \mathrm{A}, \quad \text{for } \phi = 90^\circ \tag{2}$$

where A is a constant [29]. The ideal λ/2 slot antenna with infinite sheet dimensions has an omnidirectional radiation pattern which is nondirectional in the yz-plane (E-plane) and bidirectional in the xz-plane (H-plane) [30]. On the other hand, in the case that the slot antenna has finite sheet dimensions, the radiated fields are generated from not only the slot aperture, but also the left and right sides parallel to the slot. The E-plane electric-field pattern of the slot antenna with finite sheet dimensions is theoretically represented at far-field observations by [28]

$$|E_{EP}(\theta)| \approx \sqrt{1 + 4b\cos\ \beta d\ \cos(\beta d \sin\theta)}, \quad \text{for } \phi = 90^\circ \tag{3}$$

where the subscript EP stands for element pattern, b is the amplitude constant of each image field generated from both sides parallel to the slot aperture, β is the wave number at 28 GHz, and d is the distance between the slot aperture and the sides [29]. Contrary to the ideal slot antenna, the designed slot antenna with finite sheet dimensions has a bidirectional pattern in the yz-plane (E-plane) and a quasi-nondirectional pattern in the xz-plane (H-plane) [31].

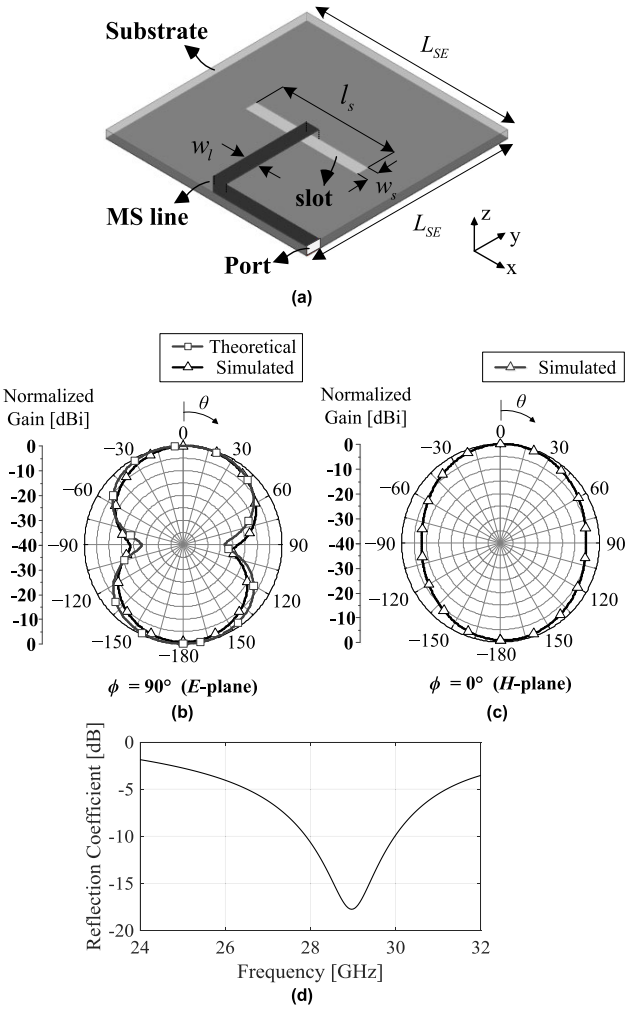

FIGURE 4. Designed slot antenna element with finite sheet dimensions: (a) the 3-D configuration and the normalized (b) E-plane and (c) H-plane gain patterns and (d) the reflection coefficient.

The 3-D configuration of the designed slot antenna with finite sheet dimensions is presented in Fig. 4(a). The designed slot antenna was implemented on an ARLON/AD430 substrate with a dielectric constant (ε_r) of 4.3, a loss tangent (δ) of 0.003, and a thickness of 0.2 mm. On the top side of the substrate, the 50 Ω microstrip (MS)- line of which the initial part is in contact with the ideal lumped port is placed to feed the slot aperture. The $\lambda_g/2$ slot cut in a conducting sheet with a size of about 1 λ_g^2 is disposed on the bottom side of the substrate, where λ_g is the guide wavelength on the 50 Ω MS-line at 28 GHz (i.e., 6 mm). The design parameters are set as $L_{\mathrm{SE}} = 5.625$ mm, $l_{\mathrm{s}} = 3.15$ mm, $w_{\mathrm{s}} = 0.32$ mm, and $w_{\mathrm{l}} = 0.36$ mm. The normalized gain patterns of the designed slot antenna are shown in Figs. 4(b) and (c). The theoretical result for the E-plane pattern in Fig. 4(b) is calculated based on Eq. (3).

The simulated results were obtained using ANSYS/HFSS software [32]. The simulated results coincide with theoretical results (see Fig. 4(b)). The simulated maximum gain and half-power beam width (HPBW) are 4.67 dBi and 75.6°,

respectively. The designed slot antenna element has a reflection coefficient of less than −10 dB over the frequency range of 27.9 GHz–30 GHz, as shown in Fig. 4(d).

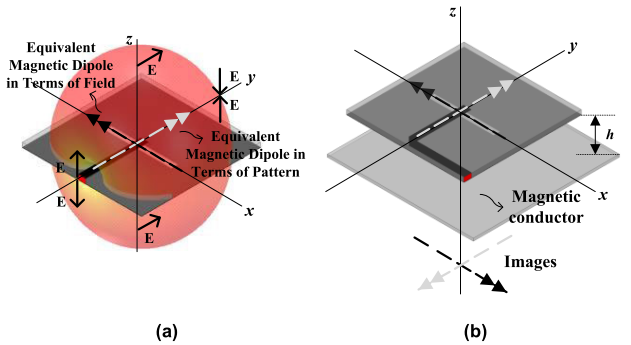

FIGURE 5. Radiation and field patterns and equivalent sources of the finite slot antennas: (a) with and (b) without the magnetic conductor reflector.

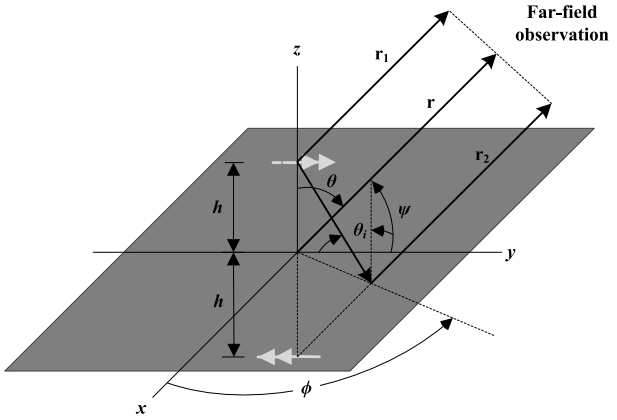

FIGURE 6. Analytical problem equivalent to the magnetic-conductor-backed slot antenna in terms of the radiation pattern.

2) AMC-BACKED SLOT ANTENNA

In this subsection, we discuss the structure in which a magnetic conductor is disposed below the slot antenna based on theoretical analysis. Ultimately, we will demonstrate how the proposed AMC-backed phased array could meet the required specifications for the subarray design in the next section. The configurations, radiation pattern, electric field distributions, and equivalent sources for a slot antenna without the AMC surface are given in Fig. 5(a). In terms of the generated E-field vectors which rotate on the xz-plane, the equivalent magnetic dipole source can be regarded to lie on the y-axis (see the black arrow in Fig. 5(a)). However, in terms of the formed radiation pattern, which is omnidirectional, the equivalent magnetic dipole source is considered to be in the direction of the x-axis (see the light gray arrow in Fig. 5(a)). From these perspectives, in the case where the magnetic conductor is placed below the designed slot antenna, the virtual sources (images) would be formed as in Fig. 5(b). That is, the images lie in a horizontal position with a 180° polarity difference relative to the sources (i.e., having a reflection coefficient (R_h) of −1), which is based on image theory [33]. Thus, from the perspective of the radiation pattern, we can replace the designed magnetic-conductor-backed slot antenna with the simple and equivalent analytical problem depicted in Fig. 6. The equivalent problem consists of real and virtual λ/2 horizontal magnetic dipole sources and an infinite magnetic conductor sheet, and each source has separation distance (h) from the magnetic conductor. Here, λ is the wavelength at 28 GHz. The total electric fields of this equivalent problem at far-field observations are represented by the sum of the direct and reflected electric field components by real and virtual dipole sources, respectively. Thus, the total E-fields are denoted by

$$E_\psi^t = E_\psi^d + E_\psi^r \simeq -j\frac{I_m e^{-jkr}}{2\pi r}\{\frac{\cos[(\pi/2)\cdot\sin\theta\sin\phi]}{\sqrt{1-\sin^2\theta\sin^2\phi}}\}\cdot(2j\sin(kh\cos\theta)),\quad z>0 \tag{4}$$

$$E_\psi^t = 0,\ z<0 \tag{5}$$

where

$$E_\psi^d = -j\frac{I_m e^{-jkr_1}}{2\pi r_1}\{\frac{\cos[(\pi/2)\cos\psi_1]}{\sin\psi_1}\} \tag{6}$$

$$E_\psi^r = -R_h j\frac{I_m e^{-jkr_2}}{2\pi r_2}\{\frac{\cos[(\pi/2)\cos\psi_2]}{\sin\psi_2}\} = j\frac{I_m e^{-jkr_2}}{2\pi r_2}\{\frac{\cos[(\pi/2)\cos\psi_2]}{\sin\psi_2}\} \tag{7}$$

$$\cos\psi = \hat{\mathbf{a}}_y\cdot\hat{\mathbf{a}}_r = \sin\theta\sin\varphi \tag{8}$$

$$\sin\psi = \sqrt{1-\cos^2\psi} = \sqrt{1-\sin^2\theta\sin^2\phi} \tag{9}$$

For far-field observations

$$r_1 \simeq r - h\cos\theta,\quad r_2 \simeq r + h\cos\theta \quad \text{for phase variations} \tag{10}$$

$$r_1 \simeq r_2 \simeq r,\quad \theta_1 \simeq \theta_2 \simeq \theta \quad \text{for amplitude variations} \tag{11}$$

Here, I_m is the magnetic current, k is the wavenumber at 28 GHz [33], [34]. Equation (4) takes the form of the product of the single element pattern of the λ/2 magnetic dipole and the factor, depending on the allocation of real and image sources. Thus, the key design parameter for optimizing the pattern shape without deformation of the element pattern is the distance h.

The normalized gain patterns calculated based on Eq. (4) for the yz- and xz-planes (i.e., the H- and E- planes) using different h values are presented in Fig. 7. In both planes, when $h = 0.25\ \lambda$, the peak relative gain arises in the boresight direction (i.e., $\theta = 0°$). As h increases within the range from λ/4 to λ/2, the gain pattern progressively spreads to both sides and the power at $\theta = 0°$ gradually decreases. When $h = 0.44\ \lambda$, the peak gain appears at $\theta = \pm 45°$ and a null appears at $\theta = 0°$. The calculated

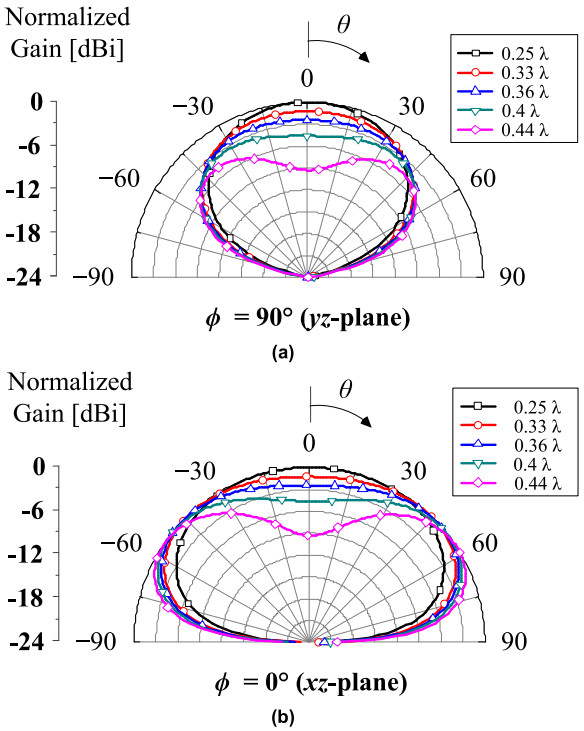

FIGURE 7. Normalized gain patterns calculated based on Eq. (4) using different h values in the (a) yz- and (b) xz-planes.

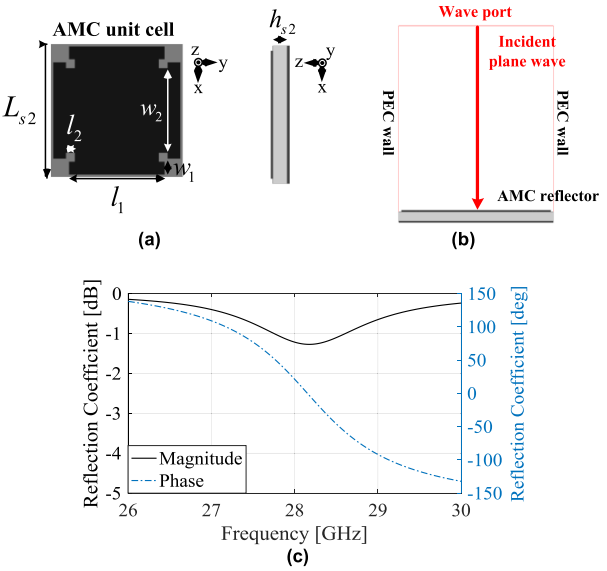

FIGURE 8. Designed AMC surface: (a) the unit-cell configuration, (b) the simulation set-up for evaluation, and (c) the simulation results for magnitude and phase of the reflection coefficient.

beamwidths in the E-plane for the threshold normalized gain of -5 dBi are 88°, 96°, 98°, and 98°, respectively, when $h = 0.25\ \lambda$, $0.33\ \lambda$, $0.36\ \lambda$, and $0.4\ \lambda$. On the other hand, the calculated values in the H-plane are 136°, 148°, 152°, and 154°, respectively, for those h values. The beamwidths in the yz-plane are on average 52.5° wider than those in the xz-plane, so the elements were designed to be arranged along the y-axis to provide better spatial coverage efficiency. Consequently, the optimized value for the design parameter h is $0.4\ \lambda$, where the widest beamwidth and a moderate gain at $\theta = 0°$ appear. The maximum relative gain arises at $\theta = \pm 37°$ in this case. Thus, if eliminating half of the H-plane pattern appropriately, the presented AMC-backed slot antenna would meet the required wide inclined elevation beam. This will be dealt with more specifically in the section IIB.

The unit cell configuration of the designed AMC surface is illustrated in Fig. 8(a). The Jerusalem Cross (JC)-shape, with its advantages in size and angular stability, is applied to the AMC design [35]. The designed AMC unit cell is implemented on a Taconic TLY substrate with a dielectric constant (ε_r) of 2.2 and a loss tangent (δ) of 0.0009, and dimensions of 5.625 mm × 5.625 mm × 0.127 mm. Here, the JC-shaped conductor is implemented on the top side of the substrate, while the bottom side is totally covered by the conductor sheet. To act as a good magnetic conductor around 28 GHz, the design parameters are set as $l_1 = 2.54$ mm, $l_2 = 0.24$ mm, $w_1 = 0.33$ mm, and $w_2 = 2.23$ mm. The simulation set-up for evaluating the responses of the AMC surface composed of the designed AMC unit cells is given in Fig. 8(b). To be able to assume an infinite arrangement of the AMC unit cells, the front and back sides of the box marked with the red line were set to the perfect magnetic conductor boundary, and the left and right sides were set to the perfect electric conductor (PEC) boundary. The top side was set to the wave port [36]. The full-wave electromagnetic simulation results are given in Fig. 8(c). As a result, the reflection phase of the designed AMC surface is 0° at 28.3 GHz, +90° at 27.47 GHz, and −90° at 29.12 GHz. Thus, the operating bandwidth of the designed AMC surface is 1.65 GHz (i.e., 6% bandwidth). The magnitude of the reflection coefficient is less than −1.5 dB over the overall frequency band.

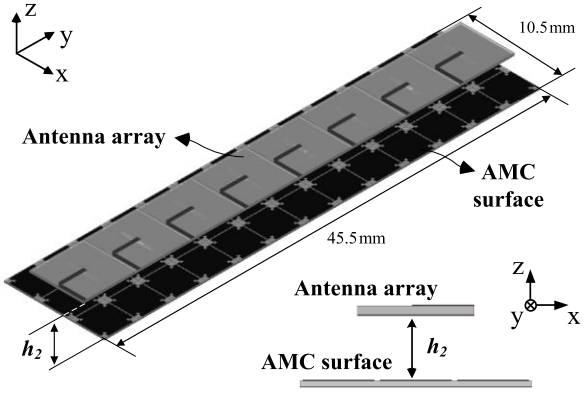

FIGURE 9. Configuration of the designed AMC-backed slot antenna array.

B. ANTENNA ARRAY DESIGN

The 3-D configuration of the designed AMC backed slot antenna array is presented in Fig. 9. The designed array consists of the slot array with eight-elements and the AMC

surface with 3 × 13 unit cells. The antenna elements are uniformly spaced with an electrical length of λ/2 along the *y*-axis. In this case, the separation distance between the array and the AMC surface is set to h_2. The overall dimensions of the designed AMC-backed antenna array are 10.5 mm × 45.5 mm × 2.2 mm. For simplicity of the expression for the electric field, it is assumed that the AMC surface has infinite dimensions and perfect reflection. Thus, the analytical electric field pattern of the designed array can be represented by

$$E_{AP}(\theta) \simeq E^t_{\psi} \cdot \Big(\sum_{m=1}^{M=8} |A_m|\, e^{j\phi_m} e^{j\frac{2\pi}{\lambda} y_m \sin\theta}\Big), \quad \text{for } \phi = 90^\circ \tag{12}$$

where

$$y_m = (m - 0.5(M+1))d_s \tag{13}$$

Here, E^t_{ψ} denotes the electric field of the single antenna element defined by Eq. (4), which is identical for each element in the array. The number of the array elements is denoted by M, and A_m and ϕ_m represent the magnitude and phase of the input voltage excited to the m-th antenna element, respectively. The function y_m denotes the position of m-th antenna element on the y-axis, while d_s represents the distance between the elements and, here, is set to be λ/2.

To verify our theoretical analysis and to evaluate the performance of the array, several simulation results are presented. The simulated gain patterns in the *xz*-plane for different h_2 values are presented in Fig. 10(a). It is noted that in the *xz*-plane, the radiation pattern of the designed array has the same shape as that of the single element. That is, with regard to the theoretical analysis shown in Fig. 7(b), similar trends are seen in Fig. 10(a). When $h_2 = 0.18\ \lambda$ or 0.22 λ, the designed structure provides boresight patterns with a maximum gain of 13.6 dBi and beamwidth of 124° for the 8 dBi threshold gain. As h_2 increases, as in the case of the theoretical analysis in Fig. 7(b), the main beam in the *xz*-plane spreads to both sides. Consequently, when $h_2 = 0.31\ \lambda$, the optimized *xz*-plane gain pattern with a maximum gain of 11.8 dBi and a beamwidth of 150° is obtained. The simulated FBR is 13.92 dB in this case. The simulated gain patterns in the *yz*-plane are presented in Fig. 10(b). The array beam patterns for scan angles (θ_s) of 0°, 10°, 20°, 30°, and 40° were plotted by controlling the phase difference between two signals excited to adjacent antenna elements ($d\phi_m = \phi_{m+1} - \phi_m$), as shown in Table 1, where the excited signals have a linearly progressive phase distribution. The amplitude of each signal is set to a constant of +1. In Fig. 10(b), the peak gains are higher than 10 dBi and the side-lobe levels (SLLs) are less than −10 dB for all scan angles.

Synthesizing the beam patterns for opposite scan angles (i.e., −40°, −30°, −20°, and −10°) is straightforward. Thus, this beam-steering property is enough to meet the azimuth coverage requirement in the range from −45° to +45°. The simulated S-parameters are given in Fig. 11, where the

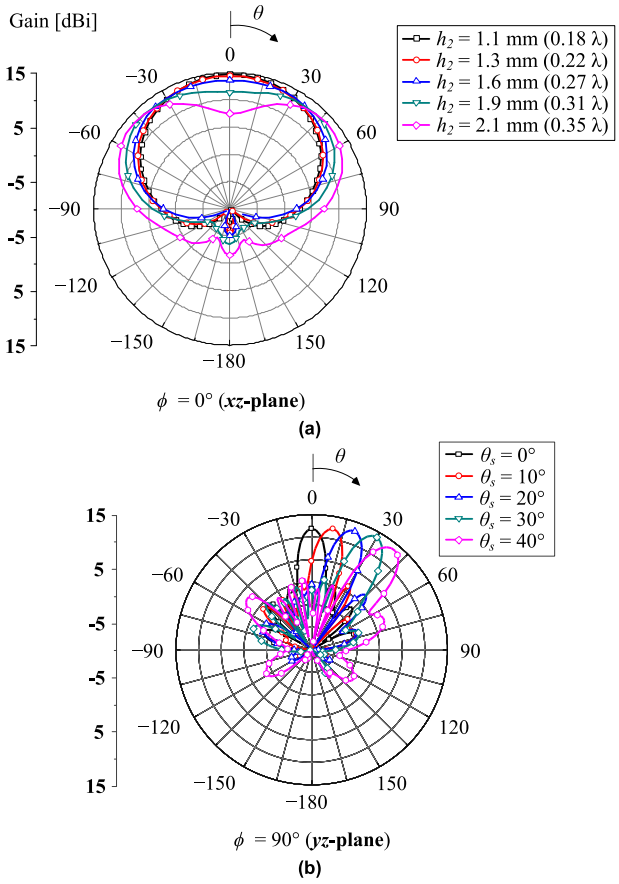

FIGURE 10. Simulated gain patterns of the designed AMC-backed slot antenna array at 28 GHz: (a) in the *xz*-plane for different h_2 values, and (b) in the yz-plane for different beam scan angles (θ_s).

TABLE 1. Phase difference between adjacent elements for beam scan angles.

Scan Angle (θ_s)	Phase difference ($d\phi_m$)	Scan Angle (θ_s)	Phase difference ($d\phi_m$)
0°	−0°	−10°	0°
10°	−60°	−20°	60°
20°	−80°	−30°	80°
30°	−100°	−40°	100°
40°	−120°		

reflection coefficients and the mutual couplings are plotted in Figs. 11(a) and (b), respectively. The simulated −10 dB S_{11} and S_{77} bandwidths are 1.64 GHz (27.85–29.49 GHz) and 1.18 GHz (27.96–29.14 GHz), respectively, which are the best and worst cases among the reflection coefficients. As shown in the reflection coefficients, extra resonances at frequencies higher than the slot antenna's resonant frequency of 28.3 GHz appear. A similar phenomenon was observed in [37]–[40]. Because of the presence of an AMC surface, the effective thickness of the substrate becomes larger, which causes the input reactance to be more capacitive [37]. The capacitive effect occurs over the frequency ranges of 28.64 GHz – 29.12 GHz and 29.6 GHz – 32 GHz in the

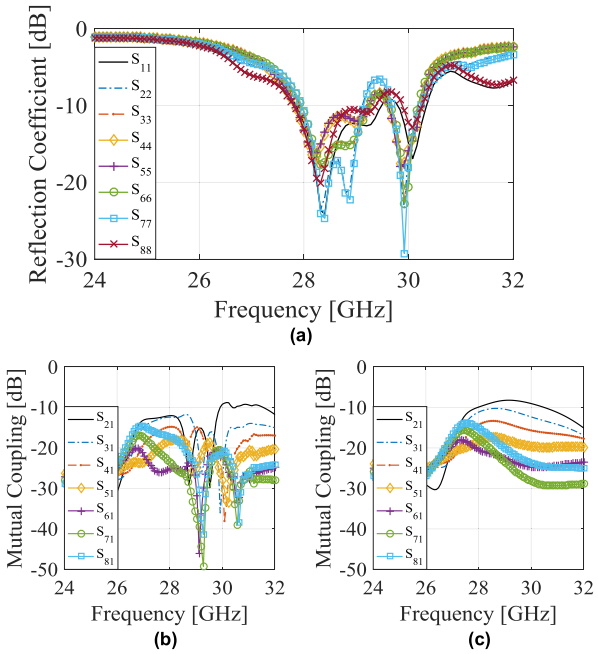

FIGURE 11. (a) Simulated reflection coefficients of the designed AMC-backed slot antenna array and the mutual couplings when using (b) AMC, and (c) PEC reflectors.

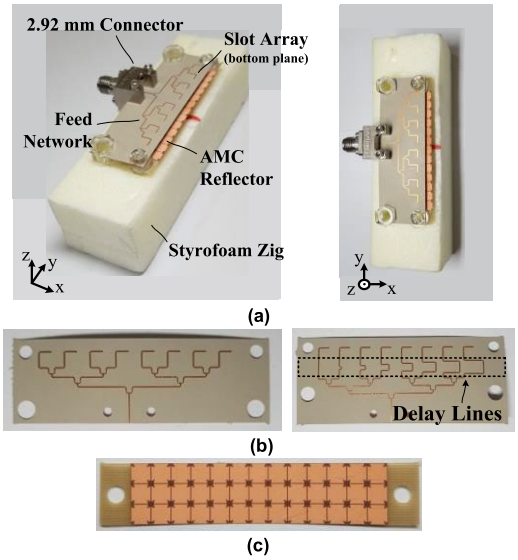

FIGURE 12. Photographs of the fabricated subarray prototype: (a) 3-D view, (b) feed networks with and without delay lines, and (c) the fabricated AMC reflector.

simulation result of the input reactance. The reason for this extra resonance especially at the higher frequencies is that the AMC surface becomes capacitive at frequencies higher than its resonant frequency of 28.3 GHz, as shown in Fig. 8. The capacitive AMC surface can store electric energy to compensate for the magnetic energy stored in the near field of the slot antenna element's source [38]. Therefore, additional zero reactance is produced at higher frequencies by loading the AMC surface. The simulated mutual couplings from

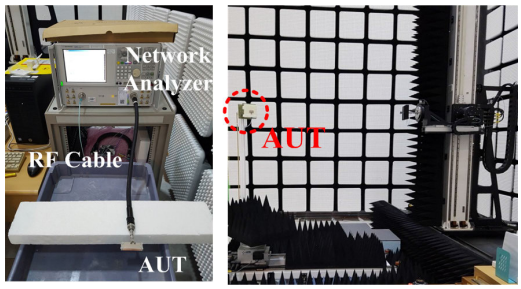

FIGURE 13. Experiment set-up for measuring the gain pattern and the reflection coefficient of the fabricated subarray prototype.

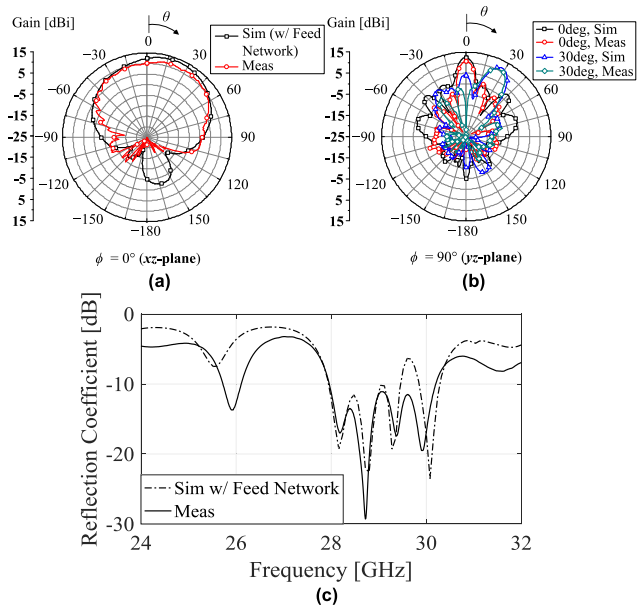

FIGURE 14. Comparison of measured and simulated results from the fabricated subarray prototype for the gain patterns at 28 GHz in (a) the *xz*-plane and (b) the *yz*-plane, and (c) the reflection coefficients.

port #1 to all other ports of the designed AMC backed array (i.e., S_{21}, $S_{31}\ldots S_{81}$) are less than -10 dB. If using a perfect electric conductor (PEC) reflector instead of the AMC reflector in the proposed array design, S_{21} exceeds -10 dB, as shown in Fig. 11(c). The reason why the mutual couplings with the AMC reflector are higher than those with the PEC reflector is that the AMC surface suppresses the excited surface waves between antenna elements owing to its high surface impedance property, unlike the PEC surface, as described in [41], [42]. The calculated radiation efficiency coefficient of the designed array is 0.77 at 28 GHz, despite using the AMC reflector.

To verify the simulation results and to evaluate the performances for the designed subarray antenna, we fabricated and measured an antenna prototype. Photographs of 3-D and top views for the fabricated subarray prototype are shown in Fig. 12(a). In the proposed design, the slots are implemented on the ground plate which is positioned on the bottom side of the upper substrate in the prototype, and the

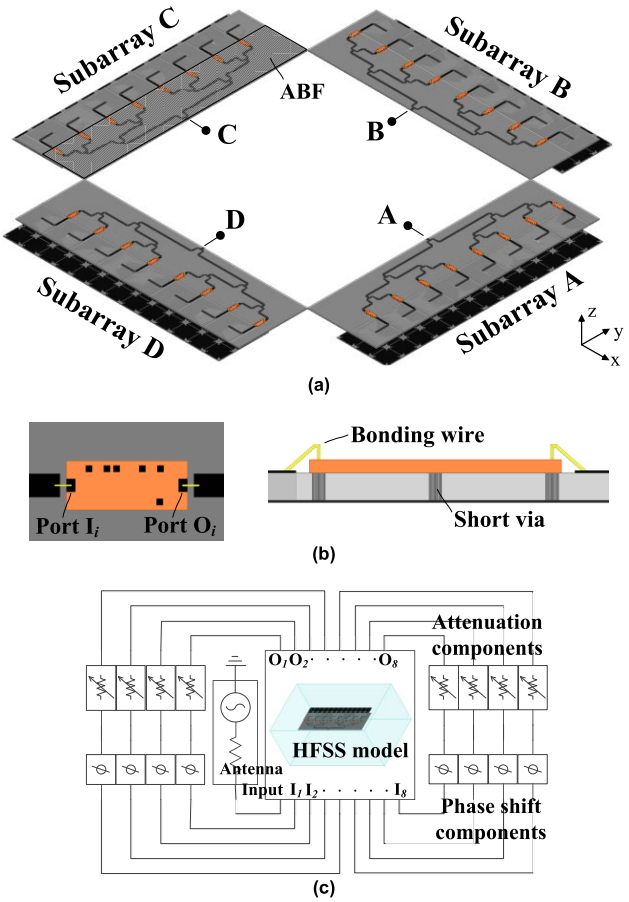

FIGURE 15. The overall structure of the proposed hemispherical-coverage phased array antenna unit, (b) the interconnection configuration of the mounted phase shifter chip, and (c) the dynamic link co-simulation environment of Ansys's HFSS and Designer for imitating chip properties through behavior models.

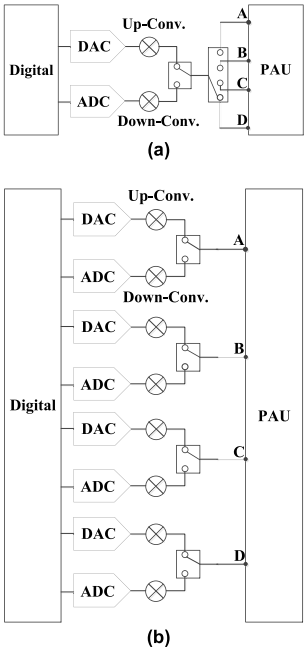

FIGURE 16. System block diagrams for (a) switched analog beamforming and (b) hybrid analog and digital beamforming.

microstrip coupled feed lines are printed on the top side of the substrate. Additionally, a feed network, which consists of seven two-way T-junction power dividers, is included in the upper substrate of the prototype to properly feed all of the antenna elements in the array (see Fig. 12(a)). This extends the dimension of the upper substrate of the prototype to the negative x-direction, which reduces the gains at the half side of the xz-plane; this indicates the reason for employing the four-subarray configuration in which each subarray covers one quarter of the hemispherical area, in the proposed phased array unit instead of the two-subarray configuration. To further assess the beam-steering performance, fixed microstrip line delays for synthesizing the beam with a specific scan angle (here, $\theta_s = 30°$) are employed in the feed network as in [6], [43]–[45] (see Fig. 12(b)). Southwest Microwave's end-launch 2.92 mm K-type connector was equipped for measurement. A photograph of the fabricated AMC reflector prototype is shown in Fig. 12(c). The experiment set-ups for measuring the gain pattern and the reflection coefficient are presented in Fig. 13. Keysight's E8362B network analyzer and MTG's near-field scanner with a standard open-ended waveguide probe were used for measurement inside an anechoic chamber at the national IT industry promotion agency, Incheon, South Korea. The measured gain patterns of the fabricated prototype are given in Figs. 14(a) and (b). These patterns were compared to the simulated results which were conducted again while including the added feed network. In the measured xz-plane gain pattern, the peak gain is 11.62 dBi which arises at $\theta = +34°$ (see Fig. 14(a)). Over the positive θ angle ranges of 0° – 62° and 0° – 90° in the xz-plane, the gains were above the 8 dBi and 1 dBi threshold levels, respectively. As pointed out earlier, the gains over the negative θ angle range of $-180°$ – 0° are reduced due to obstructing the reflected wave from the AMC surface by the addition of the feed network in the prototype design. The measured and simulated results agree well. In the measured yz-plane gain pattern, the peak gains were 10.6 dBi and 10.3 dBi for the 0° and 30° beam scans, respectively. As a result, it can be seen that the synthesized array beam pattern of the fabricated prototype is well-formed in the yz-plane, and that the measured result also agrees well with the simulation. The measured and simulated reflection coefficients of the designed subarray are presented in Fig. 14(c) and are less than -10 dB over the targeted frequency range of 28 GHz – 29 GHz.

III. HEMISPHERICAL COVERAGE PHASED ARRAY UNIT

In this section, the overall structure of the proposed hemispherical-coverage phased array antenna unit based on the subarray design is introduced, and its performance is evaluated. As shown in Fig. 15(a), the proposed phased array unit consists of four identical designed subarrays, which intuitively matches the design concept diagram depicted

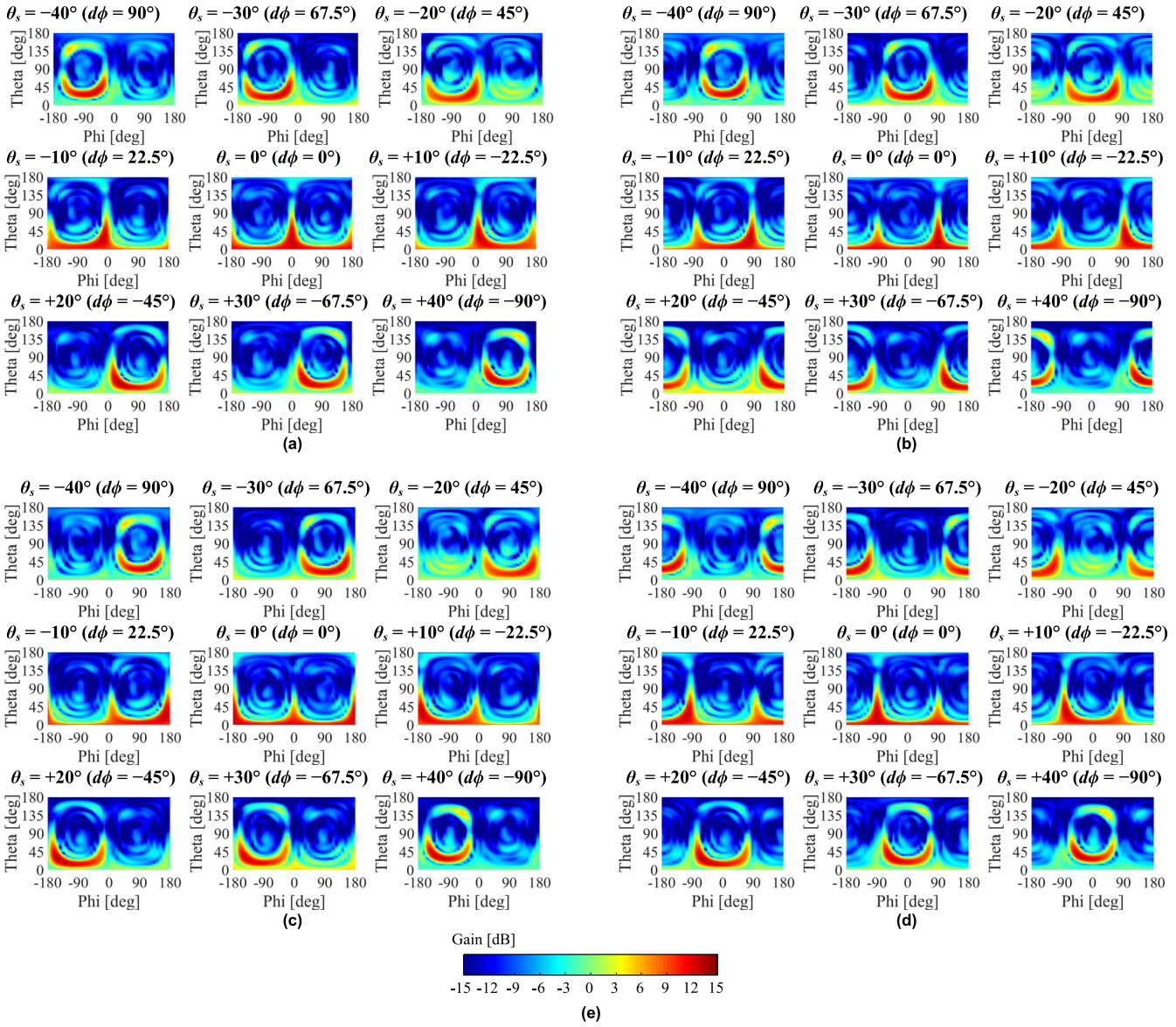

FIGURE 17. The gain patterns for different beam scan angles with intervals of 10° for each subarray in the proposed hemispherical-coverage phased array unit at 28 GHz: (a) subarray A, (b) subarray B, (c) subarray C, (d) subarray D, and (e) the legend.

in Fig. 2. The dimensions of the overall structure are 80.8 mm × 80.8 mm × 2.4 mm. In this structure, for implementation of more practical beamforming, 5-bit CMOS phase shifters (Triquint's TGP-2100 [46]) are assumed to be included instead of the fixed delay lines, as in [47]. The added phase shifters act as an analog-beamformer (ABF) in each subarray, together with the power dividers. Radio-frequency front-end (RFFE) circuits such as a power amplifier (PA) and a low-noise amplifier (LNA) were not included in the ABF structure because our main focus is on the angular beam-coverage. Of course, state of the art ABFs, which include RFFEs, phase shifters, and power dividers in one packaged chip, such as NXP's MMW-9002-KC [48] and Analog Devices' ADMV-4801/4821 [49], [50] can also be utilized instead of the current ABF. The expanded top and cross-sectional views for one of the mounted phase shifter chips are illustrated in Fig. 15(b). A chip having dimensions of 1.88 mm × 0.75 mm × 0.1 mm is interconnected with the microstrip lines in the ABF using gold bonding wires and shorting vias, which follows the JEDEC 4-point standard [51]. The distance between adjacent termination edges of the microstrip line and the chip is 0.1 mm, and the length of the bonding wires is 0.45 mm. The wire inductance calculated using Ansys' Q3D extractor [52] is 0.17 nH at 28 GHz, and the interconnection loss is calculated to be 0.4 dB at that frequency. However, information on the layout schematic of the commercial chip is not open to the public. To address this, behavior models for imitating the phase shift properties of the chip were utilized. For convenience, the internal loss property of the chip, which is –6 dB, was not

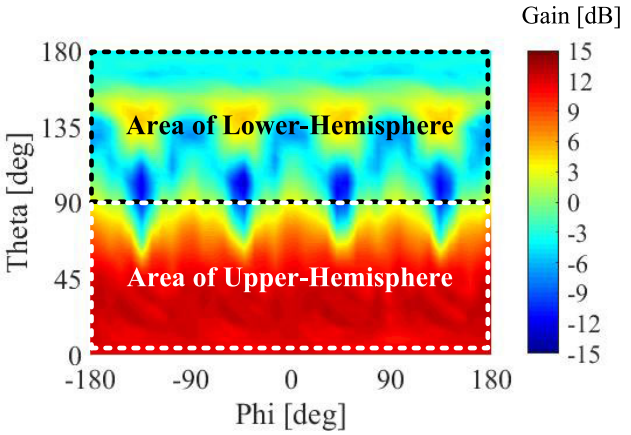

FIGURE 18. Total scan pattern of the proposed compact low-profile hemispherical-coverage phased array antenna unit consisting of four subarrays at 28 GHz.

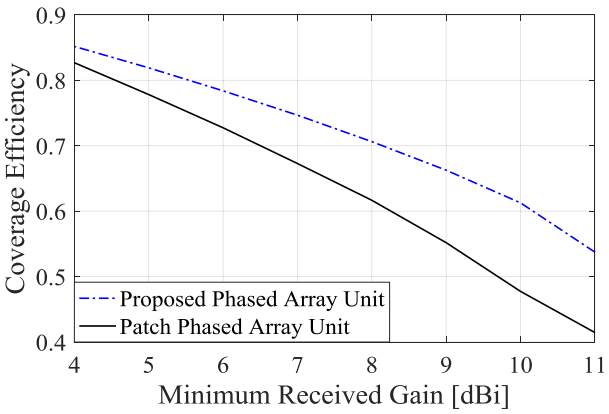

FIGURE 19. Coverage efficiencies of the proposed compact low-profile hemispherical-coverage phased array antenna unit consisting of four subarrays and the patch phased array antenna unit with the same subarray configuration and feed network at 28 GHz.

considered because it can be compensated by amplifiers in practical systems. Hence, each attenuator in Fig. 15(c) is set to be a non-activated non-model component. In using of the behavior models, dynamic link co-simulation was performed, which connects the electromagnetic solver, HFSS, with the RF circuit simulator, Ansys' Designer [53]. On the co-simulation schematic, the behavior models are positioned between each pair of lumped ports (Port I_i and Port O_i) of the HFSS model, as shown in Figs. 15(b) and (c). The solved HFSS model, the phase shifter components, and the signal source are included in the co-simulation schematic for one subarray. The system integration example of the proposed phased array unit (PAU) for beamforming is given in Fig. 16. In general, digital processors, analog-to-digital converters (ADCs), digital-to- analog converters (DACs), up/down converters with RF switches for the time division duplex (TDD), and PAUs including ABFs compose the overall 5G mm-wave system [54], [55]. In the case of fully analog systems that support one data stream instantaneously, the subarrays in the proposed phased array unit can be implemented in such that they can be switched using a SP4T switch (see Fig. 16(a)). In the case of analog-digital hybrid systems that can provide multi-data streams at the same time, the subarrays can be directly connected to the up/down converters (see Fig. 16(b)).

For each subarray of the proposed phased array unit, the gain patterns generated by different beam scans ranging from $-40°$ to $+40°$ with an interval of $10°$ are presented in Fig. 17. Here, the phase difference $d\phi_m$ is set to have a step of 22.5°, which is the available resolution in 5-bit phase shifters. For all beam scans, the simulated maximum gains of each subarray are higher than 12.4 dBi. Additionally, the FBRs of each subarray are less than -10 dB for most of the beam scans except for the $\pm 40°$ case. Moreover, it is seen that all of the designed subarrays cover each quarter of the upper hemisphere with moderate gains. The total scan pattern for the proposed phased array unit is shown in Fig. 18, which refers to the pattern extracted to the highest gain at every angular distribution point (θ, ϕ) among all array patterns with different beam scans [10]. As a result, the proposed phased array unit could cover almost the entire area of the upper hemisphere with proper gains. The calculated coverage efficiency (η_c) is presented in Fig. 19, and is defined as

$$\eta_c = \frac{\text{Coverage Solid Angle}}{\text{Maximum Solid Angle}}\bigg|_{\text{gain}} \tag{14}$$

where the coverage solid angle is calculated using the total scan pattern higher than a certain gain, and the maximum solid angle is 2π steradians because a hemisphere is chosen. The coverage efficiencies of the proposed phased array antenna unit for threshold gains of 5 dBi, 8 dBi, and 10 dBi are 0.82, 0.71, and 0.61, respectively, which is increased by 0.04, 0.09, and 0.13, respectively, over the phased array antenna unit constructed for comparison consisting of patch antenna elements introduced in [56] which have a gain of 6 dBi and the same subarray configuration and feed network.

IV. CONCLUSION

In this paper, we propose a compact low-profile phased array antenna unit with unidirectional hemispherical beam-coverage for 5G mm-wave applications such as V2I/HST/A2G communications, wireless APs, and small-cell BTSs. We devised the four subarray configuration to achieve unidirectional hemispherical coverage in the boresight direction normal to the structure, and described the design considerations for each subarray. Here, each subarray is required to have a steerable beam over a range within $\pm 45°$ in the azimuth plane, and a wide inclined beam with a 90° beamwidth in the elevation plane.

We propose an AMC-backed slot antenna array with eight elements as a solution for the subarray design. By choosing the optimal distance between the AMC surface and the antenna elements, the elevation beamwidth of the proposed array is enlarged by 20% compared to

the non-optimized case. To verify the simulation results, we fabricated a prototype for the proposed subarray and performed measurements. It was shown that the simulated and measured results agree well with each other with few errors. The fabricated subarray prototype has a peak gain of 11.62 dBi and a gain above 8 dBi over the positive θ angles of 0°–62° in the measured *xz*-plane. For the 30° beam scan, the measured *yz*-plane gain pattern is well formed.

Finally, we present the overall structure of the proposed compact low-profile hemispherical-coverage phased array antenna unit consisting of four subarrays. The dimensions of the overall structure are 80.8 mm × 80.8 mm × 2.4 mm. In this structure, commercial 5-bit CMOS phase shifters are included for more practical beam-steering achieved by performing dynamic link co-simulation. As a result, the coverage efficiencies of the proposed phased array antenna unit for the threshold gains of 5 dBi, 8 dBi, and 10 dBi are 0.82, 0.71, and 0.61, respectively, which is increased by 0.04, 0.09, and 0.13, respectively over the conventional patch phased array antenna unit. Moreover, the proposed array unit is proven to be compact and low-profile and to have high gains, enlarged elevation beamwidths, good scattering parameters, FBRs, and a beam-steering property.

REFERENCES

[1] S.-Y. Lien, S.-L. Shieh, Y. Huang, B. Su, Y.-L. Hsu, and H.-Y. Wei, "5G new radio: Waveform, frame structure, multiple access, and initial access," *IEEE Commun. Mag.*, vol. 55, no. 6, pp. 64–71, Jun. 2017.

[2] N. Javaid, A. Sher, H. Nasir, and N. Guizani, "Intelligence in IoT-based 5G networks: Opportunities and challenges," *IEEE Commun. Mag.*, vol. 56, no. 10, pp. 94–100, Oct. 2018.

[3] *User Equipment (UE) Radio Transmission and Reception; Part 2: Range 2 Standalone (Release 15)*, document TS38.101-2 v15.0.0, Jun. 2018.

[4] A. I. Sulyman, A. T. Nassar, M. K. Samimi, G. R. Maccartney, T. S. Rappaport, and A. Alsanie, "Radio propagation path loss models for 5G cellular networks in the 28 GHZ and 38 GHZ millimeter-wave bands," *IEEE Commun. Mag.*, vol. 52, no. 9, pp. 78–86, Sep. 2014.

[5] B. Rupakula, S. Zihir, and G. M. Rebeiz, "Low complexity 54–63-GHz transmit/receive 64-and 128-element 2-D-scanning phased-arrays on multilayer organic substrates with 64-QAM 30-Gbps data rates," *IEEE Trans. Microw. Theory Techn.*, vol. 67, no. 12, pp. 5268–5281, Dec. 2019.

[6] J. Bang and J. Choi, "A SAR reduced mm-wave beam-steerable array antenna with dual-mode operation for fully metal-covered 5G cellular handsets," *IEEE Antennas Wireless Propag. Lett.*, vol. 17, no. 6, pp. 1118–1122, Jun. 2018.

[7] X. Gu, D. Liu, C. Baks, O. Tageman, B. Sadhu, J. Hallin, L. Rexberg, P. Parida, Y. Kwark, and A. Valdes-Garcia, "Development, implementation, and characterization of a 64-element dual-polarized phased-array antenna module for 28-GHz high-speed data communications," *IEEE Trans. Microw. Theory Techn.*, vol. 67, no. 7, pp. 2975–2984, Jul. 2019.

[8] A. H. Aljuhani, T. Kanar, S. Zihir, and G. M. Rebeiz, "A scalable dual-polarized 256-element Ku-band phased-array SATCOM receiver with ±70° beam scanning," in *IEEE MTT-S Int. Microw. Symp. Dig.*, Jun. 2018, pp. 1203–1206.

[9] J. Helander, D. Sjoberg, M. Gustafsson, K. Zhao, and Z. Ying, "Characterization of millimeter wave phased array antennas in mobile terminal for 5G mobile system," in *Proc. IEEE Int. Symp. Antennas Propag. USNC/URSI Nat. Radio Sci. Meeting*, Vancouver, BC, Canada, Jul. 2015, pp. 7–8.

[10] J. Helander, K. Zhao, Z. Ying, and D. Sjoberg, "Performance analysis of millimeter-wave phased array antennas in cellular handsets," *IEEE Antennas Wireless Propag. Lett.*, vol. 15, pp. 504–507, 2016.

[11] I. Syrytsin, S. Zhang, G. F. Pedersen, and A. S. Morris, "Compact quad-mode planar phased array with wideband for 5G mobile terminals," *IEEE Trans. Antennas Propag.*, vol. 66, no. 9, pp. 4648–4657, Sep. 2018.

[12] M. M. Samadi Taheri, A. Abdipour, S. Zhang, and G. F. Pedersen, "Integrated millimeter-wave wideband end-fire 5G beam steerable array and low-frequency 4G LTE antenna in mobile terminals," *IEEE Trans. Veh. Technol.*, vol. 68, no. 4, pp. 4042–4046, Apr. 2019.

[13] N. Ojaroudiparchin, M. Shen, S. Zhang, and G. Pedersen, "A switchable 3-D-coverage-phased array antenna package for 5G mobile terminals," *IEEE Antennas Wireless Propag. Lett.*, vol. 15, pp. 1747–1750, 2016.

[14] M. Stanley, Y. Huang, H. Wang, H. Zhou, A. Alieldin, and S. Joseph, "A capacitive coupled patch antenna array with high gain and wide coverage for 5G smartphone applications," *IEEE Access*, vol. 6, pp. 41942–41954, 2018.

[15] M. Abdullah, X. Chen, Q. Li, and T. A. Khan, "A 28 GHz switchable 3-D coverage millimeter-wave phased array antenna for 5G handset terminals," in *Proc. Eur. Microw. Conf. Central Eur. (EuMCE)*, Prague, Czech Republic, May 2019, pp. 423–426.

[16] S. Zhang, X. Chen, I. Syrytsin, and G. F. Pedersen, "A planar switchable 3-D-coverage phased array antenna and its user effects for 28-GHz mobile terminal applications," *IEEE Trans. Antennas Propag.*, vol. 65, no. 12, pp. 6413–6421, Dec. 2017.

[17] J. Zhang, S. Zhang, X. Lin, Y. Fan, and G. Pedersen, "3D radiation pattern reconfigurable phased array for transmission angle sensing in 5G mobile communication," *Sensors*, vol. 18, no. 12, p. 4204, Nov. 2018.

[18] B. Sadhu, C. W. Baks, D. Liu, D. Friedman, A. Valdes-Garcia, J.-O. Plouchart, H. Ainspan, A. K. Gupta, M. Ferriss, M. Yeck, M. Sanduleanu, and X. Gu, "A 250-mW 60-GHz CMOS transceiver SoC integrated with a four-element AiP providing broad angular link coverage," *IEEE J. Solid-State Circuits*, vol. 55, no. 6, pp. 1516–1529, Jun. 2020, doi: 10.1109/JSSC.2019.2943918.

[19] A. L. Amadjikpe, D. Choudhury, C. E. Patterson, B. Lacroix, G. E. Ponchak, and J. Papapolymerou, "Integrated 60-GHz antenna on multilayer organic package with broadside and end-fire radiation," *IEEE Trans. Microw. Theory Techn.*, vol. 61, no. 1, pp. 303–315, Jan. 2013.

[20] J. Zhang, S. Zhang, Z. Ying, A. S. Morris, and G. F. Pedersen, "Radiation-pattern reconfigurable phased array with p-i-n diodes controlled for 5G mobile terminals," *IEEE Trans. Microw. Theory Techn.*, vol. 68, no. 3, pp. 1103–1117, Mar. 2020.

[21] G. Noh, J. Kim, H. Chung, and I. Kim, "Realizing multi-gbps vehicular communication: Design, implementation, and validation," *IEEE Access*, vol. 7, pp. 19435–19446, 2019.

[22] V. Va, T. Shimizu, G. Bansal, and R. W. Heath, "Beam design for beam switching based millimeter wave vehicle-to-infrastructure communications," in *Proc. IEEE Int. Conf. Commun. (ICC)*, May 2016, pp. 1–6.

[23] F. Hasegawa, A. Taira, G. Noh, B. Hui, H. Nishimoto, A. Okazaki, A. Okamura, J. Lee, and I. Kim, "High-speed train communications standardization in 3GPP 5G NR," *IEEE Commun. Standards Mag.*, vol. 2, no. 1, pp. 44–52, Mar. 2018.

[24] L. Zhang, H. Zhao, S. Hou, Z. Zhao, H. Xu, X. Wu, Q. Wu, and R. Zhang, "A survey on 5G millimeter wave communications for UAV-assisted wireless networks," *IEEE Access*, vol. 7, pp. 117460–117504, 2019.

[25] F. Firyaguna, J. Kibilda, C. Galiotto, and N. Marchetti, "Performance analysis of indoor mmWave networks with ceiling-mounted access points," *IEEE Trans. Mobile Comput.*, early access, Feb. 7, 2020, doi: 10.1109/TMC.2020.2972282.

[26] A. Naqvi and S. Lim, "Review of recent phased arrays for millimeter-wave wireless communication," *Sensors*, vol. 18, no. 10, p. 3194, Sep. 2018.

[27] H. G. Booker, "Slot aerials and their relation to complementary wire aerials (Babinet's principle)," *J. Inst. Electr. Eng. IIIA: Radiolocation*, vol. 93, no. 4, pp. 620–626, 1946.

[28] J. D. Kraus, *Antennas*, 2nd ed. New York, NY, USA: McGraw-Hill, 1988.

[29] Radio Research Laboratory, *Very High-Frequency Techniques*. New York, NY, USA: McGraw-Hill, 1947.

[30] S. Nikolaou, "Design of reconfigurable annular slot antenna (ASA) for wireless communications/WLAN applications," M.S. thesis, Dept. Elec. Comp. Eng., Georgia Inst. Tech., Atlanta, GA, USA, 2005.

[31] M. Cryan, S. Helbing, F. Alimenti, P. Mezzanotte, L. Roselli, and R. Sorrentino, "Simulation and measurement of quasi-optical multipliers," *IEEE Trans. Microw. Theory Techn.*, vol. 49, no. 3, pp. 451–464, Mar. 2001.

[32] *Ansys HFSS, ver. 2016.2*, Ansys Corporation, Pittsburgh, PA, USA, 2017.

[33] C. A. Balanis, *Antenna Theory: Analysis and Design*, 3rd ed. Hoboken, NJ, USA: Wiley, 2005.

[34] C. A. Balanis, *Advanced Engineering Electromagnetics*, 2nd ed. Hoboken, NJ, USA: Wiley, 2012.

[35] H. R. Raad, A. I. Abbosh, H. M. Al-Rizzo, and D. G. Rucker, "Flexible and compact AMC based antenna for telemedicine applications," *IEEE Trans. Antennas Propag.*, vol. 61, no. 2, pp. 524–531, Feb. 2013.
[36] M. K. T. Al-Nuaimi and W. G. Whittow, "Low profile dipole antenna backed by isotropic Artificial Magnetic Conductor reflector," in *Proc. 4th Eur. Conf. Antennas Propag. (EuCAP)*, Apr. 2010, pp. 1–5.
[37] M. S. Alam, N. Misran, B. Yatim, and M. T. Islam, "Development of electromagnetic band gap structures in the perspective of microstrip antenna design," *Int. J. Antennas Propag.*, vol. 2013, pp. 1–22, 2013.
[38] G. Li, H. Zhai, L. Li, C. Liang, R. Yu, and S. Liu, "AMC-loaded wideband base station antenna for indoor access point in MIMO system," *IEEE Trans. Antennas Propag.*, vol. 63, no. 2, pp. 525–533, Feb. 2015.
[39] M. E. De Cos and F. Las-Heras, "Troubleshooting RFID Tags Problems with Metallic Objects Using Metamaterials," in *Current Trends Challenges RFID*. Rijeka, Croatia: InTech Open Access Publisher, pp. 171–184, 2011. [Online]. Available: https://www.intechopen.com/ books/current-trends-and-challenges-in-rfid/troubleshooting-rfid-tags -problems-with-metallic-objects-using-metamaterials.
[40] A. Joshi and R. Singhal, "Probe-fed wideband AMC-integrated hexagonal antenna with uniform gain characteristics for WLAN applications," *Wireless Netw.*, vol. 26, no. 5, pp. 3569–3578, Jul. 2020.
[41] F. Capolino, Ed., *Metamaterials Handbook: Applications of Metamaterials*. Boca Raton, FL, USA: CRC Press, 2009.
[42] E. Young Kim, J. Hwan Yoon, Y. Joong Yoon, and C. Gu Kim, "Low profile dual-band reflector antenna with dual resonant AMC," in *Proc. IEEE Int. Symp. Antennas Propag. (APSURSI)*, Jul. 2011, pp. 1800–1803.
[43] S. X. Ta, H. Choo, and I. Park, "Broadband printed-dipole antenna and its arrays for 5G applications," *IEEE Antennas Wireless Propag. Lett.*, vol. 16, pp. 2183–2186, May 2017.
[44] J.-Y. Shim, J.-G. Go, and J.-Y. Chung, "A 1-D tightly coupled dipole array for broadband mmWave communication," *IEEE Access*, vol. 7, pp. 8258–8265, 2019.
[45] Y. Hong and J. Choi, "60 GHz patch antenna array with parasitic elements for smart glasses," *IEEE Antennas Wireless Propag. Lett.*, vol. 17, no. 7, pp. 1252–1256, Jul. 2018.
[46] *TGP-2100 Data Sheet*, TriQuint, Hillsboro, OR, USA, Aug. 2008.
[47] O. Abari, H. Hassanieh, M. Rodreguiz, and D. Katabi, "Poster: A millimeter wave software defined radio platform with phased arrays," in *Proc. 22nd Annu. Int. Conf. Mobile Comput. Netw.*, New York, NY, USA, Oct. 2016, pp. 419–420.
[48] *MMW-9002-KC Data Sheet*, NXP semiconductors, Eindhoven, The Netherland.
[49] *ADMV 4801 Data Sheet*, Analog Devices, Norwood, MA, USA, 2020.
[50] *ADMV 4821 Data Sheet*, Analog Devices, Norwood, MA, USA, 2020.
[51] *Bond Wire Modeling Standard*, EIA/JEDEC Standard EIA/JESD59, Jun. 1997.
[52] *ANSYS Q3D Extractor, ver. 2017.2*, Ansys Corporation, Pittsburgh, PA, USA, 2018.
[53] *ANSYS Designer, ver. 2017.2*, Ansys Corporation, Pittsburgh, PA, USA, 2018.
[54] T. Cameron, "Bits to beams: RF technology evolution for 5G millimeter wave radios," Tech. Rep., Analog Devices, Norwood, MA, USA, 2018. [Online]. Available: https://www.analog.com/en/technical-articles/bits-to-beams-rf-technology-evolution-for-5g-millimeter-wave-radios.html
[55] B. Peterson and D. Schnaufer, "5G fixed wireless access array and RF front-end trade-offs," *Microw. J.*, vol. 57, no. 2, pp. 22–43, Feb. 2018.
[56] *SAM-2832830695-DM-L1-64C Data Sheet*, Eravant, Torrance, CA, USA, 2020.

JIHOON BANG is currently pursuing the M.S. and Ph.D. degrees with the Department of Electronics and Computer Engineering, Hanyang University, Seoul, South Korea. His research interests include antenna design, microwave circuit and system design, and EMC/EMI.

JAEHOON CHOI (Senior Member, IEEE) received the B.S. degree from Hanyang University, Seoul, South Korea, in 1980, and the M.S. and Ph.D. degrees from Ohio State University, Columbus, OH, USA, in 1986 and 1989, respectively. From 1989 to 1991, he was a Research Analyst with the Telecommunication Research Center, Arizona State University, Tempe, AZ, USA. From 1991 to 1995, he was a Team Leader of the Satellite Communication Division, Korea Telecom. Since 1995, he has been a Professor with the Department of Electrical and Computer Engineering, Hanyang University. He has published more than 200 peer-reviewed journal articles and contributed to numerous conference proceedings. He also holds over 50 patents. His research interests include antennas, microwave circuit design, and EMC.